

Stiffness Modelling for One Curvic Coupling Considering Contact Details



Cheng Yang, Dayi Zhang, Yifei Dou, and Jie Hong

Abstract Curvic couplings have been widely used in precise mechanical devices at high loading and high rotate speed, such as aircraft engines, because of its high torque transmission capacity and precise auto centering. So far, most stiffness models for curvic couplings are created to implement the qualitative stiffness analysis, neglecting the detailed features and the contact stiffness, which limit their precision. In this study, the stiffness analysis of curvic couplings is simplified as the plane-strain problem, to determine both the tensile–compressive stiffness of one tooth, taking into account their detailed features, and contact stiffness. All possible deformation factors: tooth deformation, dedendum deformation, flange deformation and contact deformation of the tooth surface are included during stiffness modelling. Based on the M-B elastic–plastic fractal model of rough contact interfaces, the contact stiffness is introduced. The non-uniform distributed load and the contact status on the tooth surface are obtained by adopting the finite-element method. In addition, the effects of the uniformly distributed load and the non-uniformly distributed load on the deformation of the curvic couplings are studied using a local equivalent stiffness model. And then, the deformation distribution on the tooth surface is solved to build two tensile–compressive stiffness models under different distributed load. The theoretical stiffness models show that the axial compression deformation of the tooth is the most influential factor at the pitch circle of the curvic coupling, followed by the contact deformation, and others have little influence. Therefore, it is necessary to consider the effect of the contact status and the compression load in the stiffness analysis of the curvic couplings, in particular for double-row large-radius arc curvic

C. Yang · D. Zhang (✉) · Y. Dou · J. Hong

School of Energy and Power Engineering, Beihang University, Beijing 100083, People's Republic of China

e-mail: dayi@buaa.edu.cn

D. Zhang · J. Hong

Beijing Key Laboratory of Aero-Engine Structure and Strength, Beijing 100191, People's Republic of China

J. Hong

Collaborative Innovation Center of Advanced Aero-Engine, Beijing 100191, People's Republic of China

© Springer Nature Singapore Pte Ltd. 2021

E. J. Sapountzakis et al. (eds.), *Proceedings of the 14th International*

Conference on Vibration Problems, Lecture Notes in Mechanical Engineering,

https://doi.org/10.1007/978-981-15-8049-9_37

couplings with short bolts. The results of the tensile–compressive stiffness constitutive model and the unit-sector finite-element model under different distributed load are compared. The result shows that the nonlinearity stiffness of the curvic coupling is mainly determined by the uneven distribution of the contact stress. Under the non-uniform load distribution of the tooth surface, the compression stiffness of the curvic coupling increases as the axial pressure increases. On the contrary, the compressive stiffness, which is obviously larger than the tensile stiffness, decreases as the axial tension increases. Although all possible factors have been considered in the improved analytical modeling, the stiffness of tooth surface is four times higher than that of the verified simulation finite-element results. Therefore, the authors don't recommend the constitutive modelling way to obtain curvic couplings stiffness, which is much more complex and not precise enough either. It can be better to model it in the phenomenological ways using experiments data, and the verified finite-element model is also better than the constitutive model.

Keywords Curvic couplings · Stiffness modeling · Contact stiffness · Non-uniformly distributed load

1 Introduction

Curvic couplings, one special hirth coupling structure used for jointing the crankshaft of aircraft engines, were designed and manufactured by the Gleason Corporation during the World War Two. After that, curvic couplings have been widely applied in precise mechanical devices at high loading and high rotate speed, such as aero-engines, high power locomotives, indexing devices, because of the advantages of high torque transmission capacity and precise auto centering.

Curvic couplings in aero-engines can be divided into two types. One type is single-row curvic couplings with long bolts and tie rod, mainly applied in turboshaft aero-engines and turboprop aero-engines. The other is double-row curvic couplings with short bolts, mainly applied in turbofan aero-engines. The double-row curvic couplings can withstand high torque and achieve precise auto centering even at high temperature. They are suitable for element structures, making aero-engines easy to disassemble and assemble, and have been used in aero-engines such as RB199 long before. In order to accurately obtain the vibration response of rotor systems, it is necessary to study the local stiffness model of curvic couplings.

The main research idea of curvic couplings stiffness models came from the researches of the common gear and the spline joint structure at earlier stage. The tooth deformation is generally divided into three parts in the gear stiffness analysis [1, 2]. The first part is tooth deformation, being analyzed by the plane-strain model or the plane-stress model [3]. The second part is tooth root deformation, being analyzed by the empirical formula of the cantilever beam model with rounded corners at the constraint. The third part is contact deformation of the tooth surface, which is

analyzed with the semi-empirical formula proposed by Lundberg and Palmgren in 1947 when they studied the rolling rod bearing [4].

Most simplified local stiffness models of curvic couplings, neglecting the contact stiffness and the structure details, are adopted to achieve the qualitative stiffness analysis at present, due to the structural complexity. Calculating the finite-element model of curvic couplings to verify the accuracy of simple models comes next.

The stiffness models of curvic couplings can be classified into three styles according to their structural forms, including the single-tooth stiffness model, the sector stiffness model and the overall stiffness model. The single-tooth stiffness model contains the single-tooth deformation stiffness and the contact stiffness of the tooth surface. The sector stiffness model is made up of the single-tooth stiffness and the flange stiffness. Lastly, the overall stiffness model is obtained by combining the sector stiffness model, neglecting the mutual influence between different sectors.

Zeyong [5, 6] established a beam element model of the curvic couplings, assuming that the contact face without friction only transmit normal force and the shaft stiffness is axially symmetric, neglecting the influence of axial compression force. The finite-element results were used to get the coefficient of the curvic couplings stiffness matrix. Then, the single-coefficient method and the double-coefficient method were proposed to amend the precision of the stiffness coefficient. Xiang [7] established a local separation model, simplifying the contact surface of the curvic couplings into the contact surface of the ring, and considering the contact stress to be linearly distributional. The local separation of the interface that occurs in the model during the bending moment load of the structure is large enough. He also deduced the influence factors of the equivalent section inertia moment of the structure. Yuan [8] and Gao [9] put forward a developed stiffness model which takes the contact stiffness into account using the Hertz contact model and the GW model, and studied the influence of axial preload on the bending stiffness of the curvic couplings. Youyun Zhang [10] built an axial compression stiffness model of the curvic couplings considering structure details. In this model, the axial stiffness of the curvic couplings included: the cylinder stiffness, the convex stiffness and the tooth stiffness. Similar to the stiffness of bolt flange connection, the deflection angle of the cylinder was considered. It was deemed that the deflection angle is the main factor that causes the nonlinear change of the stiffness.

Bannister [11] used the finite-element method to analyze the stiffness model of the curvic couplings at the first time, and proposed to use the equivalent section inertia moment parameters to quantitatively describe the bending stiffness. The effect of the local equivalent section inertia moment and the axial section inertia moment on the dynamic characteristics of the rotor was analyzed as well. Xia [12] qualitatively researched the bilinear characteristics of the curvic couplings torsional stiffness. The result indicated that the contact stiffness had little influence on the torsional stiffness. And the bilinear stiffness characteristics were also obtained by using the nonlinear finite-element model. Liu [13] and Yeming [14] studied the bending stiffness of the curvic couplings in a hirth and a high-power locomotive using the finite-element method. They calculated the dynamic characteristics of the rotor with the curvic coupling basing on their local stiffness model as well.

For the local stiffness models of curvic couplings, most of them do not consider the impact of the contact stiffness, and also cannot reflect the impact of different axial compression conditions on the local stiffness. In this study, taking into account the detailed features of curvic couplings, the stiffness analysis of the curvic couplings is simplified as the plane-strain problem to determine both the tensile stiffness and the compressive stiffness. All the possible deformation factors are included during modelling. Based on the M-B elastic-plastic fractal model of rough contact interface, the contact stiffness is considered the influence. In addition, the effects of uniformly distributed load and non-uniformly distributed load on the deformation of the curvic coupling are studied by using the local equivalent stiffness model.

2 Theoretical Stiffness Model of Curvic Couplings

2.1 Simplified Model and Deformation Factors

Double-row curvic couplings are generally applied in the high-pressure rotor system of turbofan engines for transmitting torque and axial force between the high-pressure turbine and the high-pressure compressor. Figure 1 shows one type of typical double-row curvic couplings. They are axisymmetric; and their loading and boundary constraint are axisymmetric as well. So a local sector model can be used to replace the whole curvic couplings to study their stiffness property. Further, we just need to analyze the mechanics performance of one side, according to the geometrical symmetry of the matched curvic couplings. And then, based on the analysis result, the stiffness of the whole curvic couplings can be obtained. The local sector model can be simplified as a cantilever beam containing one tooth and one flange as shown in Fig. 1.

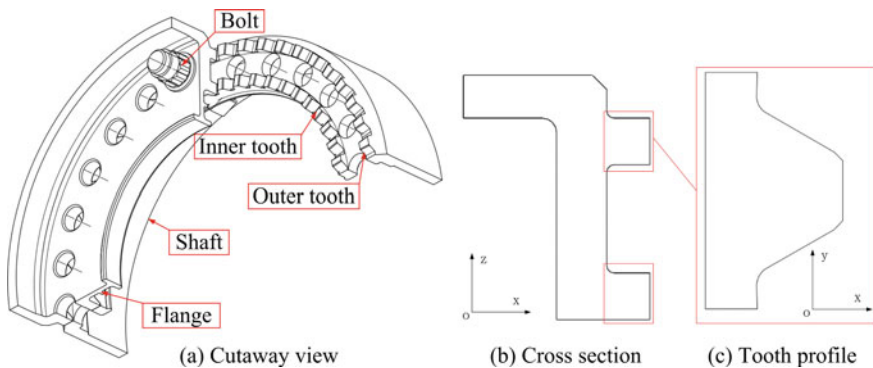


Fig. 1 Curvic couplings

For the convenience of the following discussion, it is considered that the contact deformation of tooth surface, being called contact deformation for short as well, is not included in the tooth deformation. Therefore, all deformations of the simplified model include the tooth deformation, the flange deformation and the contact deformation. The theoretical formulas for these deformations are derived based on the deep beam theory and the fractal theory. The total axial and circumferential deformation of a pair of curvic couplings, including a pair of inner teeth, a pair of outer teeth and two flanges, represented by δ_x and δ_y , are given by

$$\delta_x = 2(\delta_{xT} + \delta_{xTC} + \delta_{xG}) + \delta_{xC}, \quad (1)$$

$$\delta_y = \delta_{yTM} + \delta_{yTS} + \delta_{yC}, \quad (2)$$

where,

- δ_{xT} is the tooth axial deformation caused by the axial force;
- δ_{xTC} is the axial compensation caused by the circumferential compression of the tooth surface;
- δ_{xG} is the flange deformation;
- δ_{xC} is the axial contact deformation of a pair of tooth surfaces;
- δ_{yTM} is the tooth flexural deflection caused by the bending moment;
- δ_{yTS} is the shear deformation caused by the shear force;
- δ_{yC} is the circumferential contact deformation of a pair of tooth surfaces.

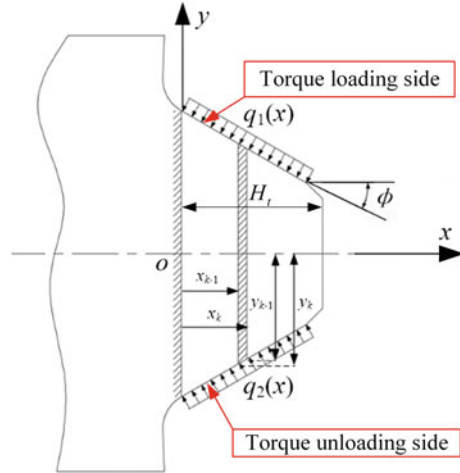
The stiffness is tangent stiffness rather than secant stiffness when the curvic couplings of the rotor vibrate laterally. Hence, the tension and compression stiffness of the curvic couplings is defined by

$$K = \frac{\Delta F}{\Delta \delta}. \quad (3)$$

2.2 Tooth Deformation

The tooth of the double-row curvic couplings is wide enough. The effective tooth length of the tooth is larger than the tooth thickness so that the plane-strain model is suitable for analyzing the tooth deformation. As shown in Fig. 2, the tooth surfaces on both sides are subjected to normal force, which is not uniformly distributed generally.

Fig. 2 Force diagram of tooth



Over here, the linear density of the normal force on the torque loading side is $q_1 = q_1(x)$, meanwhile the linear density on the torque unloading side is $q_2 = q_2(x)$. Let us set $q = q_1 + q_2$. The normal force per unit length l is ql as the tooth thickness is unit thickness.

(a) Axial deformation caused by axial force

The tooth axial deformation is analyzed at first. It is assumed that the cross-section of the tooth deforms uniformly under the normal force on tooth surfaces. The axial force F_k on the k th microsegment in Fig. 2 is expressed by

$$F_k = q(H_t / \cos \phi - x_k / \cos \phi) \sin \phi = q(H_t - x_k) \tan \phi, \tag{4}$$

where H_t is the total height of the tooth.

Then, we have the axial deformation of the k th microsegment taking the form

$$\Delta h_k = \frac{\sigma_k}{E} h_k = \frac{F_k}{A_k E_\mu} h_k, \tag{5}$$

where A_k is the average cross-sectional area of the k th microsegment, $A_k = y_{k-1} + y_k$, $y_k = y_0 - x_k \cdot \tan \phi$, W is the tooth thickness; $h_k = x_k - x_{k-1}$. The elastic modulus E needs to be modified as $E_\mu = \frac{E}{1-\mu^2}$.

In the case of the small deformation hypothesis, the tooth axial deformation caused by the axial force can be obtained by superposing linearly all microsegment deformations. Consequently, the tooth axial deformation is given by

$$\delta_{xT} = \sum_{k=1}^n \Delta h_k = \int_{x=0}^{H_t} \frac{F_k}{A_k E_\mu} dx = \int_{x=0}^{H_t} \frac{q(H_t - x) \tan \phi}{2(y_0 - x \cdot \tan \phi) E_\mu} dx. \tag{6}$$

(b) Flexural deflection caused by bending moment

The normal force on the torsional bearing side of the curvic coupling is larger than that on the non-torsional bearing side, the circumferential force difference: $\Delta q = (q_2 - q_1) \cos \phi$, causes the tooth to bend. According to the Mohr's theorem, the flexural deflection at the arbitrary point x_1 is

$$\delta_{yTM}(x_1) = \int_0^{x_1} \frac{M(x) \cdot M^0(x)}{E_\mu \cdot I(x)} dx, \tag{7}$$

where

- $M(x)$ is the bending moment along the axial direction;
- $M^0(x)$ is the bending moment caused by unit force applying at the position x_1 ;
- $I(x)$ is the moment of inertia of the tooth section.

We can calculate $M(x)$, $M^0(x)$ and $I(x)$ by

$$M(x) = \frac{1}{2} \Delta q \cdot (H_t - x)^2, \tag{8}$$

$$M^0(x) = \begin{cases} x_1 - x & x \in [0, x_1] \\ 0 & x \in (x_1, H_t] \end{cases}, \tag{9}$$

$$I(x) = \frac{2h(x)^3(a^2 + 4ab + b^2)}{9(a + b)}, \tag{10}$$

respectively. In Eq. (10), $y(x) = y_0 - x \cdot \tan \phi$; $a = R_i \psi$, $b = (R_i + \frac{l}{2}) \psi$ are the coefficients of the inner tooth; $a = (R_o - \frac{l}{2}) \psi$, $b = R_o \psi$ are the coefficients of the outer tooth; $\psi = \pi / N$ is the opening angle of the tooth. The moment of inertia of the inner and outer tooth is

$$I(x) = \frac{4(y_0 - x / \cos \phi)^3 \left[R_i^2 + 4R_i(R_i + \frac{l}{2}) + (R_i + \frac{l}{2})^2 \right] \psi^2}{9(4R_i + l)} + \frac{4(y_0 - x / \cos \phi)^3 \left[R_o^2 + 4R_o(R_o - \frac{l}{2}) + (R_o - \frac{l}{2})^2 \right] \psi^2}{9(4R_o - l)}. \tag{11}$$

Hence, the flexural deflection of the tooth can be rewritten in the more legible form

$$\delta_{yTM}(x_1) = \int_0^{x_1} \frac{\Delta q \cdot (H_t - x)^2 \cdot (x_1 - x)}{2E_\mu \cdot I(x)} dx. \tag{12}$$

(c) Shear deformation caused by shear force

The shear deformation is also caused by the circumferential force difference. The Timoshenko beam assumption that the plane is flat after deformation and the transverse deformations at the same section are equal is adopted. Under the normal force on both sides of the tooth, the shear force along the axial is given by

$$S(x) = \Delta q \cdot (H_t - x). \tag{13}$$

The shear strain energy is solved by the Castigliano’s theorem. Also, it can be expressed by

$$V_\epsilon = \int_H \frac{k_s S^2(x)}{2GA} dx \tag{14}$$

where k_s is the shear shape coefficient of the tooth section, and its value is related to both the shear stress distribution and the section shape.

The shear deformation at the arbitrary point x_2 is

$$\delta_{yTS}(x_2) = \int_0^{H_t} \frac{k_s S(x)}{GA} \frac{\partial S(x)}{\partial S(x_2)} dx, \quad \frac{\partial S(x)}{\partial S(x_2)} = \begin{cases} 1 & 0 \leq x \leq x_2 \\ 0 & x_2 < x \leq H_t \end{cases}. \tag{15}$$

Consequently,

$$\delta_{yTS}(x_2) = \int_0^{H_t} \frac{k_s S(x)}{GA} \frac{\partial S(x)}{\partial S(x_2)} dx = \int_0^{x_2} \frac{k_s S(x)}{GA} \frac{\partial S(x)}{\partial S(x_2)} dx = \int_0^{x_2} \frac{k_s \Delta q \cdot (H_t - x)}{GA} dx, \tag{16}$$

where G is the shear modulus, A is the area of the shadow trapezoid in Fig. 2, k_s is the shear shape coefficient of the trapezoid section.

A and k_s can be calculated by

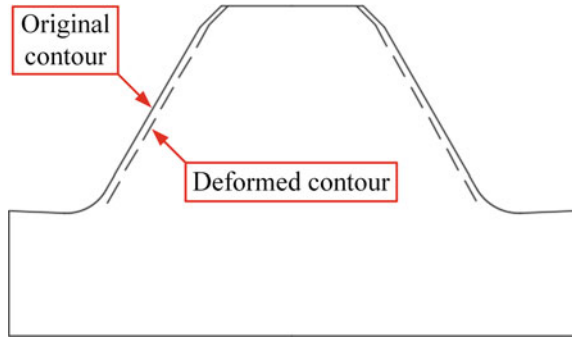
$$A = \frac{1}{2} \left(2R_i + \frac{l}{2} \right) \psi l + \frac{1}{2} \left(2R_o - \frac{l}{2} \right) \psi l, \tag{17}$$

$$k_s = \frac{8a^5 + 56a^4b + 101a^3b^2 + 61a^2b^3 + 31ab^4 + 31b^5}{30(a+b)(a^2+b^2)^2}. \tag{18}$$

(d) Axial compensation caused by circumferential load

The axial compensation is caused by the circumferential load on the tooth surface. Supposing the circumferential force distributes linearly, the circumferential force is expressed by

Fig. 3 Tooth surface compression deformation



$$F_{TC}(x, y) = q_1 dx + (q_1 - q_2) dx \frac{y - y(x)}{2y(x)}. \tag{19}$$

Thus, the following form of the circumferential compression can be deduced

$$\delta_{yTC} = \frac{F_{TC}(x, y)W}{\frac{1}{2}(2R_i + \frac{l}{2})\psi dx + \frac{1}{2}(2R_o - \frac{l}{2})\psi dx} = \frac{2q_1 y(x) + (q_1 - q_2)(y - y(x))}{[(2R_i + \frac{l}{2})\psi + (2R_o - \frac{l}{2})\psi]y(x)} W. \tag{20}$$

The circumferential compression of the tooth surface reduces the circumferential thickness of the tooth surface. The tooth should undergo an axial displacement in order to maintain the seamless fit between the tooth surfaces, as shown in Fig. 3. Hence, the axial compensation caused by the circumferential compression is

$$\delta_{xTC} = \frac{\delta_{yTC}}{\tan \phi}. \tag{21}$$

2.3 Contact Deformation of Tooth Surface

The fractal model of the M-B elastic–plastic rough contact surface considering the elastic-plasticity takes the form

$$A_r = \int_{a_s}^{a_l} n(a)ada, \tag{22}$$

where

- A_r is the real contact area;
- a is the area of a single micro-convex body after contacting;

$n(a)$ is the size distribution function of the contact point;
 a_s is the area of the maximum contact point;
 a_l is the area of the minimum contact point.

The distribution formula of the truncated area is given by

$$n(a) = \frac{D}{2} a_l^{D/2} a^{-(D/2+1)}. \tag{23}$$

From Eq. (22), we deduce the normal load and the maximum relative displacement between contact surfaces [15]

$$P = \frac{2^{(9-2D)/2} D B^{(D-1)} E^* (\ln \gamma)^{1/2}}{3\pi^{(3-D)/2} (3-2D)} (a_l'^{(3/2-D/2)} - a_l'^{D/2} a_c'^{(3/2-D)}) + \frac{HD}{2-D} a_l'^{D/2} a_c'^{(1-D/2)} \quad (1 < D < 2, D \neq 1.5) \tag{24}$$

$$P = 2\pi^{-3/4} B^{1/2} E^* (\ln \gamma)^{1/2} a_l'^{3/4} \ln(a_l'/a_c') + 3H a_l'^{3/4} a_c'^{1/4} \quad (D = 1.5)$$

$$\Delta = \delta_{\max} = 2^{(3-D)} B^{(D-1)} \pi^{-(2-D)/2} (\ln \gamma)^{1/2} (a_l')^{(2-D)/2}, \tag{25}$$

where D is the fractal dimension of the surface topography; B is the fractal roughness parameter; E^* and H represent the equivalent Young's modulus and the material hardness; γ is a constant being greater than 1.0.

According to the elastic-plastic condition, the critical truncation area can be obtained by

$$a_c = \left[\frac{2^{(7-2D)} B^{(2D-2)}}{\pi^{(1-D)} b} \left(\frac{E^*}{H} \right)^2 (\ln \gamma) \right]^{1/(D-1)}, \quad \frac{\delta_c}{\delta} = \left(\frac{a}{a_c} \right)^{(D-1)} \quad (1 < D < 2). \tag{26}$$

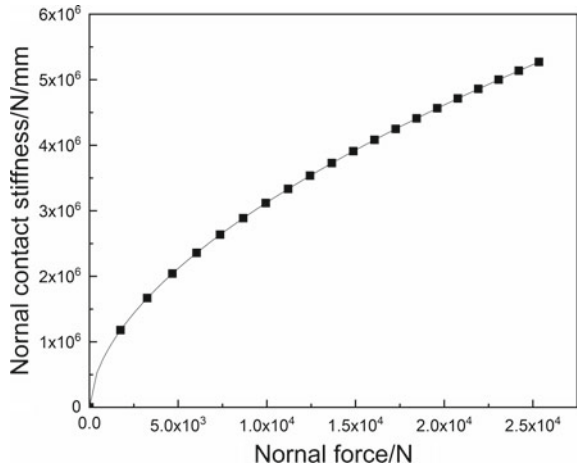
The contact stiffness K_n is defined as the partial derivative of the normal force P with respect to the maximum relative displacement Δ . So the contact stiffness K_n is

$$K_n = \frac{\partial P}{\partial \Delta}. \tag{27}$$

The fractal parameters D and B of the rough surface in the formula adopt the equivalent parameter values of general milling contact pairs: $D = 1.2183$, $B = 5.9036E - 14$. The material parameters of the contact surface are the mechanical parameters of 1Cr18Ni9Ti: $E = 201$ GPa, $\nu = 0.30$, $H = 200$ [16]. Thus, the normal load P and the normal stiffness K_n are related by

$$P \approx \frac{2^{(9-2D)/2} D B^{(D-1)} E^* (\ln \gamma)^{1/2}}{3\pi^{(3-D)/2} (3-2D)} a_l'^{(3/2-D/2)}, \tag{28}$$

Fig. 4 The relation between the contact stiffness and the normal force



$$K_n \approx \frac{4D(3 - D)E^*}{3\sqrt{2\pi}(3 - 2D)(2 - D)}(a_l')^{1/2}. \tag{29}$$

So far, the implicit function relation between K_n and P is obtained, as shown in Fig. 4.

The load distribution of the tooth surface can be obtained by means of the Gleason stress analysis method or the finite-element method. The contact deformation of the tooth surface can be obtained by

$$\delta_{xC} = \frac{P}{K_n(P)} \sin \phi, \tag{30}$$

$$\delta_{yC} = \frac{P}{K_n(P)} \cos \phi. \tag{31}$$

2.4 Flange Deformation

The loads on the flange mainly include the axial force component generated by the teeth and the compression force generated by the bolts, as shown in Fig. 5a, b. It is assumed that the axial forces on the inner teeth and the outer teeth are equal. Since the simplified structure is symmetric, the problem can be solved by using half of the flange, as shown in Fig. 5c. The linearly distributed force along the radial direction is q_3 ; the equivalent force at bolt hole is $q_4 = \frac{q_3 l}{R_o - R_i - l}$. Further, the loads on the flange can be seen as the superposition of the force q_4 and the force $(q_3 + q_4)$, as shown in Fig. 5d.

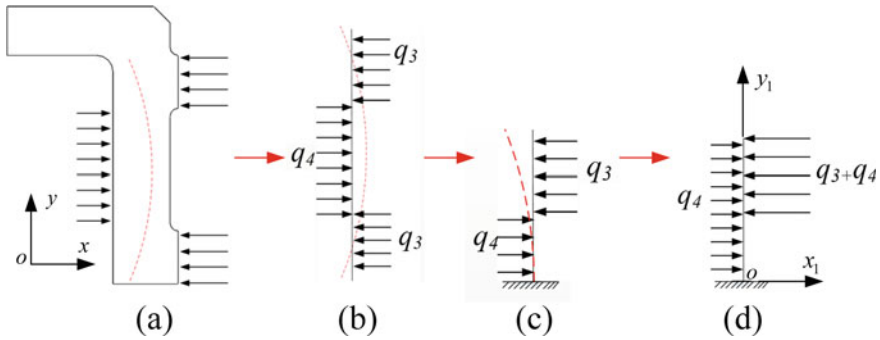


Fig. 5 Force and deformation analysis of flange

Hence, the deflection deformations of the flange under the force q_4 are given by

$$w_1 = \frac{q_4 y_1^2}{24EI} \left[2(R_o - R_i)y_1 - \frac{3}{2}(R_o - R_i)^2 - y_1^2 \right], \tag{32}$$

$$\theta_1 = w'_1 = \frac{q_4 y_1}{12EI} [2(R_o - R_i) - 2y_1]. \tag{33}$$

And then, the deflection deformations w_1 and θ_1 under the force $(q_3 + q_4)$ can be solved with the same method as well. According to the superposition principle, the total deflections of the flange are

$$w = w_1 + w_2, \tag{34}$$

$$\theta = \theta_1 + \theta_2. \tag{35}$$

The flange deformation mainly affects the axial partial deformation and the radial deformation of the curvic couplings. However, it does not cause the circumferential deformation component. Therefore, it mainly has influence on the axial stiffness of the curvic coupling. The additional axial deformation takes the form

$$\delta_{xG} = w + y(1 - \cos \theta). \tag{36}$$

3 Stiffness Characteristics Under Uniformly Distributed Load

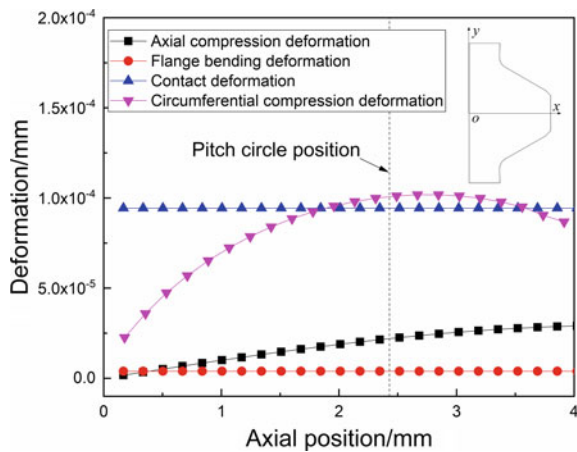
3.1 Deformation Distribution Characteristics

The axial stiffness of the curvic couplings is the major factor that influences the vibration response of the rotor system. Therefore, all the following sections are only focus on the axial stiffness. However, studying the circumferential stiffness can follow the same method. It can be seen from the theoretical stiffness model above that the factors affecting the axial stiffness include: the tooth axial compression, the axial compensation, the axial contact deformation and the flange deformation. The distribution characteristics of these four factors along the axial are analyzed below.

The tooth axial compression and the flange deformation are easy to be calculated in the theoretical analytical model. However, the axial compensation caused by the circumferential compression of the tooth surfaces is complex, and more assumptions are needed to obtain its theoretical solution. Therefore, the axial compensation is obtained by the finite-element method in this section.

Based on the theoretical model analysis we put forward and the finite-element simulation, the deformation distribution of the curvic couplings is shown in Fig. 6. In the theoretical model analysis, the bolt preload equals 20 kN and the circumferential force equals 3 kN. The axial compensation of the tooth has the greatest influence on the axial deformation at the pitch circle of the tooth, followed by the axial contact deformation; the tooth axial compression and the flange deformation have little influence. Hence, the tooth contact and the tooth surface compression must be considered in the stiffness analysis of large-radius double-row curvic couplings with short bolts. At last, the total axial deformation and the axial stiffness of the curvic couplings can be obtained as summing all the deformations.

Fig. 6 Distribution of tooth surface deformation under bolt preload



3.2 Influence of Axial Force

The torque loading side is mainly in viscous state under the normal working conditions; the torque unloading side is mainly in slip state. The loads on the tooth surface are shown in Fig. 7. The frictional force on the torque unloading side is set as the maximum static friction force: $F_{t2} = \mu F_{n2}$. Then the static equilibrium equations take the form

$$\begin{cases} F_{n1} \sin \alpha + F_{n2} \sin \alpha + F_{t2} \cos \alpha = F_x \\ F_{n1} \cos \alpha - F_{n2} \cos \alpha + F_{t2} \sin \alpha = F_y \end{cases} \quad (37)$$

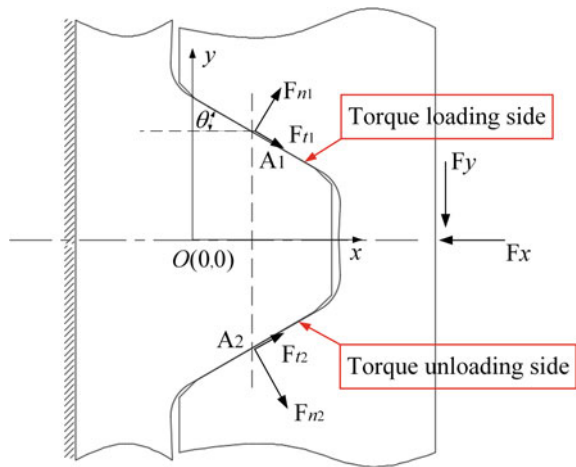
From Eq. (37), F_{n1} , F_{n2} and F_{t2} are expressed by

$$\begin{cases} F_{n1} = \frac{F_x(\cos \alpha - \mu \sin \alpha) + F_y(\sin \alpha + \mu \cos \alpha)}{\mu(\cos^2 \alpha - \sin^2 \alpha) + 2 \sin \alpha \cos \alpha} \\ F_{n2} = \frac{F_x \cos \alpha - F_y \sin \alpha}{2 \sin \alpha \cos \alpha + \mu(\cos^2 \alpha - \sin^2 \alpha)} \\ F_{t2} = \mu F_{n2} = \frac{\mu(F_x \cos \alpha - F_y \sin \alpha)}{2 \sin \alpha \cos \alpha + \mu(\cos^2 \alpha - \sin^2 \alpha)} \end{cases} \quad (38)$$

According to Eq. (38), the interface loads are linearly related to the axial force when the pressure angle and the circumferential load of the curvic coupling are determined. During studying the influence of the axial force on stiffness, this linear relation can be used to obtain the interface loads quickly, and then getting the corresponding deformation and stiffness.

We change the bolt preload in order to simulate the change of the axial force. Figure 8 shows the influence law of the bolt preload on the axial compensation, the

Fig. 7 Force analysis of curvic couplings



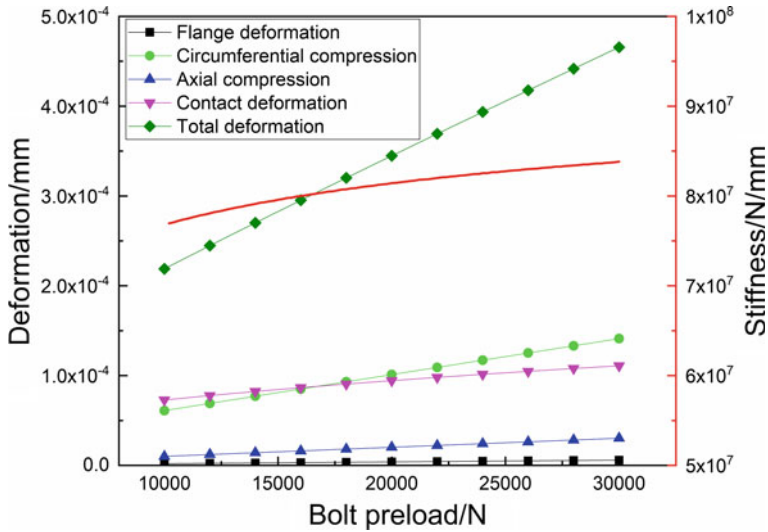


Fig. 8 Mechanical properties of curvic couplings under uniform load

axial contact deformation, the tooth axial compression and the flange deformation. By analyzing the bolt preload affecting on each part deformation, we found the nonlinear factor of the stiffness comes from the contact deformation of the tooth surface when the forces on the tooth surface are uniformly distributed. In addition, the stress at the contact interface is large enough to minimize the nonlinear of the contact stiffness, so that the nonlinear characteristics of the deformation are not obvious.

4 Stiffness Characteristics Under Non-uniformly Distributed Load

4.1 Finite-Element Model

In order to analyze the stiffness characteristics of the curvic couplings under the non-uniform load, the finite-element model of the curvic couplings was established to calculate and extract the stress distribution of the tooth surface. If all tension or compression status of the tooth surface is carried out, the computational cost is enormous. Therefore, only tension and compression state is simulated.

The curvic couplings have 48 pairs of teeth and 22 compression bolts. Due to the periodic symmetry of the model, a 1/24 sector model as shown in Fig. 9 is built and periodic symmetric boundary conditions were applied on the model. The parameter details of the full hexahedral grid model were listed in Table 1. The mechanical parameters of 1Cr18Ni9Ti are selected according to the material manual [16]. The

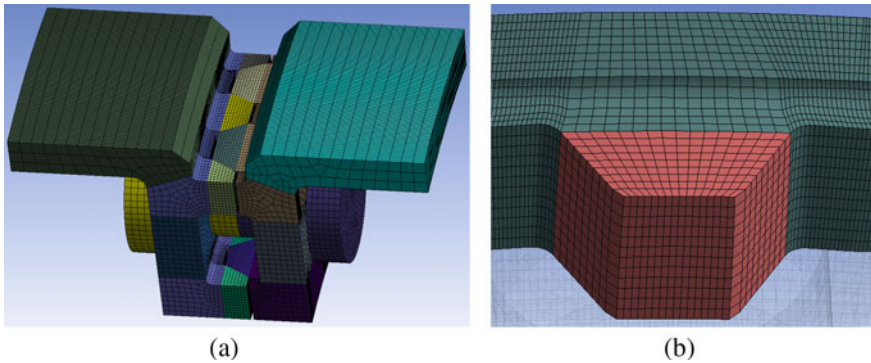


Fig. 9 Finite-element model of curvic couplings; **a** 1/24 sector model, **b** local convex tooth model

Table 1 Mechanical parameters of 1Cr18Ni9Ti

Parameter name	Parameter detail
Material	1Cr18Ni9Ti
Solid element type	Solid 186
Contact element	TARG170/CONT174
Contact friction coefficient	0.15
Contact algorithm	Penalty function method

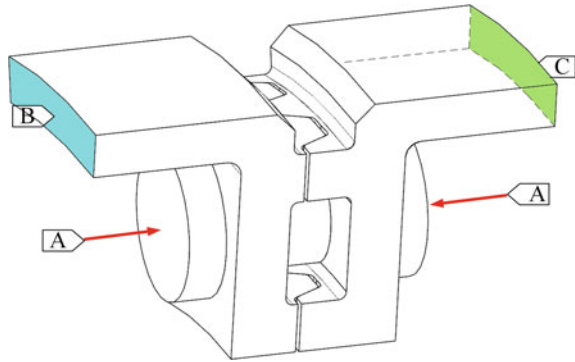
preload of the bolt is applied by PRET179 element. The element size of the flange and the shaft is 1.0 mm. The partial densification of the tooth and its root was carried out with 0.4 mm elements to accurately depict the local stress concentration of the contact surface.

The boundary conditions are shown in Table 2 and Fig. 10. The bolt preload, the torque and the axial force are applied to the model one by one in three load steps to make sure the calculation convergence. The torque is equivalent to the circumferential force. The finite-element model is a 1/24 sector model, whereas the theoretical model is a 1/48 sector model. The values of loading conditions for the finite-element model are twice larger than the values for the theoretical model.

Table 2 Boundary conditions of curvic couplings model

Boundary condition	Value
Axial displacement at B/mm	0
Circumferential displacement at B/mm	0
Bolt preload at A/kN	40
Circumferential force at C/kN	6
Axial force in tension state at C/kN	2
Axial force in compression state at C/kN	2

Fig. 10 Boundary conditions



4.2 Non-uniform Load

Figure 11 shows the stress distribution on the tooth surface. The stress of the 1–2 path with the maximum contact stress was extracted. The stress distribution under tension or compression state which is used for the following analysis is obtained by fitting the stress in Fig. 11 with a polynomial of 5 degrees.

The fitting formula of stress distribution in the tension state is

$$f_1(x) = -46.63x^5 + 679.7x^4 - 3801x^3 + 1.037 \times 10^4x^2 - 1.395 \times 10^4x + 7840. \tag{39}$$

The fitting formula of the contact stress distribution is

$$f_2(x) = -56.73x^5 + 858.3x^4 - 4910x^3 + 1.36 \times 10^4x^2 - 1.84 \times 10^4x + 10,360, \tag{40}$$

when the tooth surface is compressed.

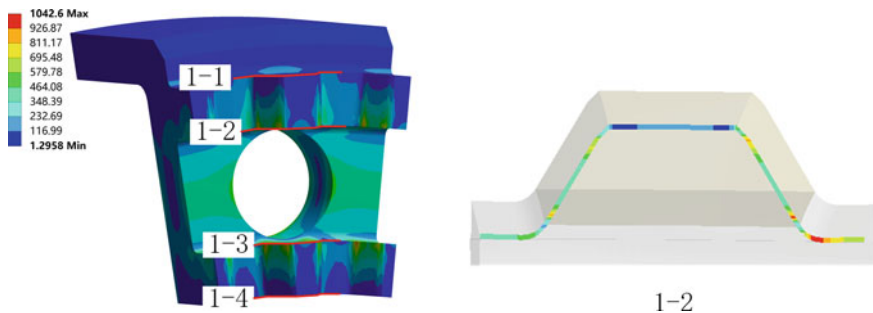
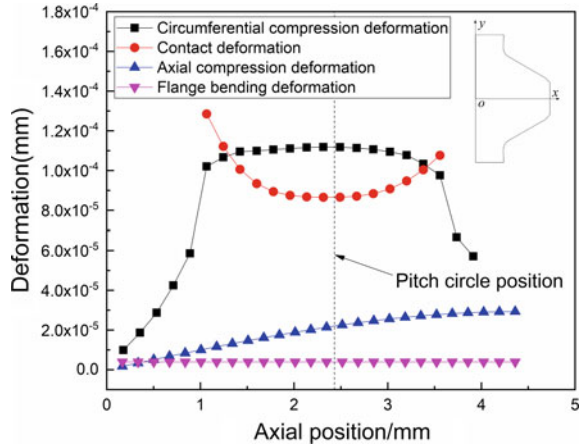


Fig. 11 Equivalent stress extraction path

Fig. 12 Deformation distribution of tooth surface under bolt preload



4.3 Deformation Distribution Characteristics

In the stiffness analytical model, the flange deformation has little influence on the stress distribution of the tooth surface, so the influence of flange deformation is ignored. Only the tooth axial compression, the axial contact deformation and the axial compensation are taken into account.

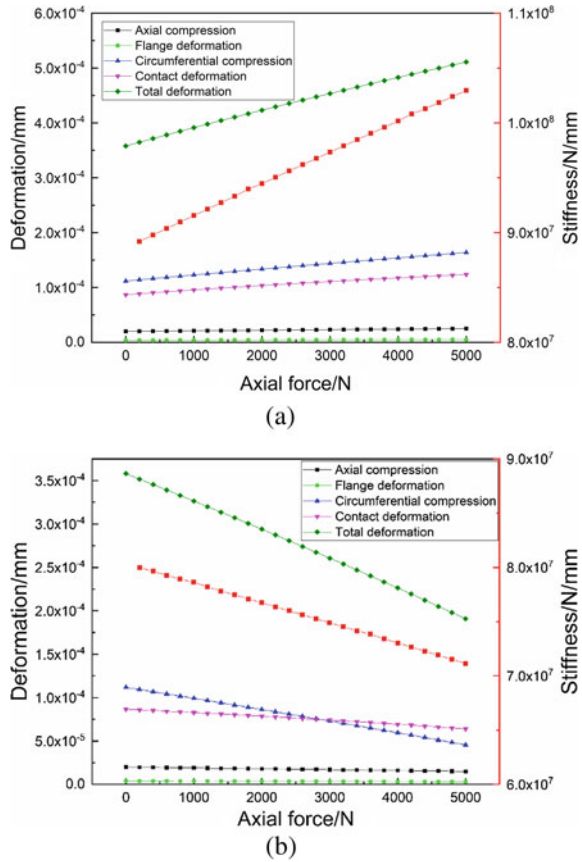
From the analysis above, the tooth surface stress distribution has a great influence on the axial contact deformation and the axial compensation at the pitch circle. Both of them are the two major factors affecting the tooth surface deformation. Hence, the stress distribution of the tooth surface has great influence on the stiffness of the curvic couplings. Figure 12 shows the tooth deformation distribution with the stress distribution taken into account. Comparing with Fig. 6, the main influence factors of the deformation are still the axial compensation and the axial contact deformation at the pitch circle, but the largest influence factor is the axial compensation.

4.4 Influence of Axial Force

After considering the stress distribution of the tooth surfaces, the tooth surface load is analyzed in the tension and compression statue, respectively. So the stiffness analysis is also conducted separately at the tension and compression statue. Basing on the finite-element model built in Sect. 4.1, the different axial forces are applied on the position C in Fig. 10. The bolt preload equals 40 kN and the circumferential force equals 6 kN.

The deformation and the stiffness of the curvic couplings relating to the axial force under tension and compression are shown in Fig. 13. The tooth axial stiffness increases with the increase of pressure when compressing the shaft; the tooth axial

Fig. 13 Mechanical properties of the curvic couplings under non-uniform load; **a** compression state, **b** tension state

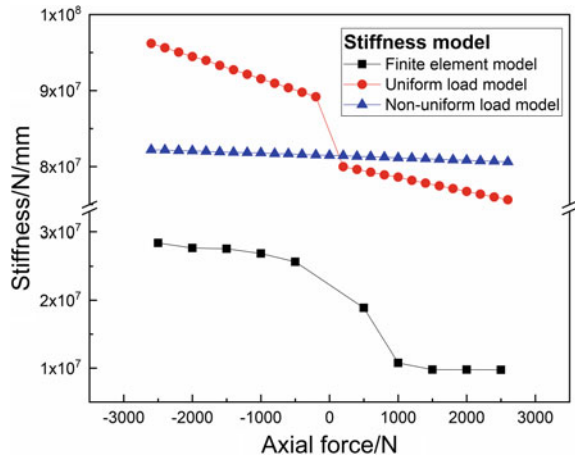


stiffness decreases with the increase of tensile force when the shaft is subjected to tension. The axial load of the teeth and the stiffness increases as the pressure increases; the axial load of the tooth and the stiffness decreases with the tension increasing. It can be concluded that the tooth stiffness increases with the axial loads of the tooth increasing, which is mainly caused by the contact stiffness of the tooth and the circumferential deformation of the tooth surface.

5 Comparison of Three Stiffness Models

In each case, the axial tension or compression forces: 1000, 2000, 3000, 4000 and 5000 N are applied on the position C in the finite-element model as shown in Fig. 10. Because a sector of the finite-element model corresponds to four pairs of teeth, the bolt preload equals 40 kN and the circumferential force equals 6 kN. The finite-element model is a 1/24 sector model, whereas the theoretical model is a 1/48 sector

Fig. 14 Comparison of three stiffness models (1/48 sector model)



model. Hence, the axial load is twice larger than that of the theoretical analysis model. In other words, the axial tension or compression forces: 500 N, 1000 N, 1500 N, 2000 N and 2500 N are applied on the 1/48 sector model, respectively.

Figure 14 shows the tensile and compressive stiffness of the theoretical model and the finite-element model under different axial loads. In Fig. 14, the negative axial load represents the compression load on the shaft, and the positive axial load represents the tensile load. It can be concluded that the nonlinearity mainly comes from the uniformly distribution of the contact stress, as the nonlinear characteristics of the curvic couplings stiffness are not obvious under uniformly distributed load. The compression stiffness of the curvic couplings is significantly higher than the tensile stiffness. The stiffness of the tooth surface is significantly higher than that of the simulation, which is about four times higher, whether or not the stress distribution on the tooth surface is taken into account.

6 Conclusions

One theoretical stiffness model for the curvic couplings considering contact details is established. The stiffness characteristics of the curvic couplings under the uniform or non-uniform load are analyzed. The results of the tensile–compressive stiffness constitutive model and the unit-sector finite-element model under different distributed load are compared. The main conclusions are as follows:

- (1) The theoretical stiffness model of the curvic couplings under the tension and compression is established, considering contact details; the influence of the non-uniform distribution of the interface contact stress is analyzed.
- (2) The axial contact deformation of the tooth and the axial compensation caused by the circumferential compression are the most important factors affecting the

stiffness of the curvic couplings, followed by the tooth axial compression and the flange deformation. The stiffness decreases with the increase of the tension load but increases with the increase of the compression load after considering the contact stress distribution at the contact interfaces.

- (3) The nonlinearity of the curvic couplings mainly comes from the non-uniform distribution of the contact stress. The compressive stiffness is obviously higher than the tensile stiffness. The theoretical model is suitable for the law study; the finite-element model is suitable for the engineering application.

References

1. Runwan L, Jianjun W (1999) Gear system dynamics. Science Press, Beijing
2. Cornell RW (1983) Compliance and stress sensitivity of spur gear teeth. *J Mech Des* 103(2):447–459
3. Marmol RA, Smalley AJ, Tecza JA (1980) Spline coupling induced nonsynchronous rotor vibrations. *J Mech Des-Trans ASME* 102(1):168–176
4. Lundberg G, Palmgren A (1947) Dynamic capacity of rolling bearings. Generalstabens Litografiska Anst. Förlag, Stockholm
5. Zeyong Y, Yuanxia O, Yuanxia L et al (1993) Stiffness of a shaft section with curvic couplings and its effect on dynamic characteristic of a rotor. *J Vib Eng* 1:63–67
6. Zeyong Y, Yuanxia O (1994) Dynamic characteristics of the rotor connected with the axial preloaded curvic couplings. *J Aero Space Power* 9(2):133–136
7. Xiang S (2013) Dynamic design method research for joint structure of turboshaft engine rotor. Beijing University of Aeronautics and Astronautics
8. Yuan S, Zhang Y, Zhu Y et al (2011) Study on the equivalent stiffness of heavy-duty gas turbines composite rotor with curvic couplings and spindle tie-bolts. American Society of Mechanical Engineers Power Division Power
9. Gao J, Yuan Q, Li P et al (2012) Effects of bending moments and pretightening forces on the flexural stiffness of contact interfaces in rod-fastened rotors. *Proc ASME Turbo Expo* 134(10):1492–1494
10. Jiang X, Zhu Y, Hong J et al (2016) Stiffness analysis of curvic coupling in tightening by considering the different bolt structures. *J Aerosp Eng* 29(3):04015076
11. Bannister RH (1980) Methods for modelling flanged and curvic couplings for dynamic analysis of complex rotor constructions. *J Mech Des* 102(1):130–139
12. Kai X, Yanhua S, Dejiang H et al (2016) Torsional characteristics of axial fastened shaft section with curvic couplings. *J Xi'an Jiaotong Univ* 50(5):51–56
13. Liu X, Yuan Q, Liu Y et al (2014) Analysis of the stiffness of hirth couplings in rod-fastened rotors based on experimental modal parameter identification, pp 26–34
14. Yeming L, Wensheng Z, Hongjun Z (2010) Performance analysis of curvic couplings of high power locomotive drive system. *Diesel Locomot* 2010(11):1–4 (in Chinese)
15. Zhang D, Xia Y, Scarpa F et al (2017) Interfacial contact stiffness of fractal rough surfaces. *Sci Rep* 7(1):12874
16. Chinese Handbook of Aeronautical Materials Committee (2002) Chinese handbook of aeronautical materials. Chinese Specification Press, Beijing